ISSN 0021-8944, Journal of Applied Mechanics and Technical Physics, 2020, Vol. 61, No. 7, pp. 1182–1193. © Pleiades Publishing, Ltd., 2020.
Russian Text © The Author(s), 2019, published in Vychislitel'naya Mekhanika Sploshnykh Sred, 2019, Vol. 12, No. 3, pp. 301–312.

Studying the Localized Shear Fracture Mechanism in Alloys under Dynamic Loading

M. A. Sokovikov[a],*, V. V. Chudinov[a],, V. A. Oborin[a],***, S. V. Uvarov[a],****, and O. B. Naimark[a],*****

[a] *Institute of Continuous Media Mechanics, Ural Branch, Russian Academy of Sciences, Perm, 614013 Russia*

**e-mail: sokovikov@icmm.ru*

***e-mail: chudinov@icmm.ru*

****e-mail: oborin@icmm.ru*

*****e-mail: usv@icmm.ru*

******e-mail: naimark@icmm.ru*

Received April 18, 2019; revised September 4, 2019; accepted September 14, 2019

Abstract—Experiments on the dynamic loading of specimens from AMg6 alloy were conducted on a split Hopkinson–Kolsky bar and with target perforation. The thermodynamics of the deformation process was studied in situ by recording temperature fields using a CEDIP Silver 450M high-speed infrared camera in order to reveal the characteristic stages of strain localization. The temperature measurements in the localization zones do not confirm the traditional concept of the strain localization mechanism caused by thermoplastic instability. Dynamic tests of specimens made of Steel 3, AMg6, and D16 alloys of a special shape designed to study the localization of plastic deformation on a split Hopkinson–Kolsky bar were conducted using the StrainMaster noninvasive strain measurement system. The displacements and strain fields in these specimens are constructed. A comparison of the experimentally measured temperature and strain fields with the results of numerical simulation with allowance for the mesodefect accumulation kinetics in the material gives a satisfactory agreement within ~20%. In the specimens after the experiments, the surface relief was analyzed using a NewView-5010 optical surface profiler with subsequent processing of the 3D strain relief data and calculation of the scale invariant (Hurst index) and the spatial scale of the region on which the correlated behavior of mesodefects is observed. The data of the experiments and analysis of the surface relief of deformed specimens, as well as the data of numerical simulation taking the mesodefects accumulation kinetics in the material into account, suggest that one of the plastic strain localization mechanisms under high-speed loading is caused by jump-wise processes in the defect structure of materials.

Keywords: plastic shear localization, dynamic loading, numerical simulation, defect structure evolution, study of the surface relief of deformed specimens

DOI: 10.1134/S0021894420070147

1. INTRODUCTION

The phenomenon of plastic strain localization, i.e., the formation of small regions of plastic flow, in which the level of plastic strain is orders of magnitude higher than in the surrounding material, is of significant theoretical and practical interest. Plastic strain localization in metals under dynamic loading is a complex process depending on the strain rate and magnitude, temperature, as well as the evolution of the structure of the material.

The two most common points of view on the causes of strain localization are thermoplastic instability and mechanisms associated with the evolution of the structure. The allowance for thermoplastic instability [1–12] made it possible to predict the initiation of shear bands, their thickness, and the distance between them in the case of their multiple occurrence. In [13, 14] it was shown that the behavior of a material under dynamic loading is determined by the state of the microstructure (grain size, distribution of their orientation, dislocation density, dislocation substructures, etc.). In [15, 16], the formation mechanism of plastic flow bands at high strain rates correlates with the processes in the microstructure of the material. In [17–19], it was stated that dynamic fracture during shear of crystalline solids can be caused by structural transitions (dynamic recrystallization).

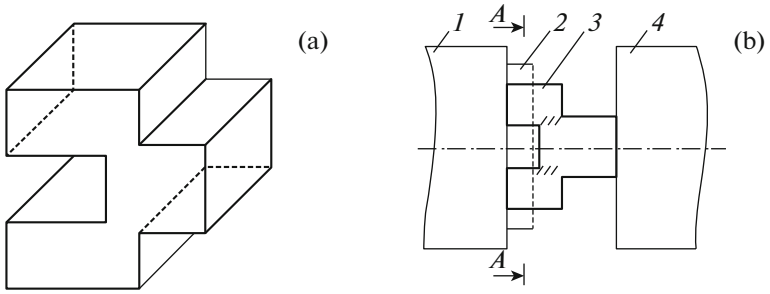

Fig. 1. (a) A specimen of special form and (b) diagram of its loading on a Hopkinson–Kolsky bar: (*1*) incident bar, (*2*) frame, (*3*) specimen (shaded areas are in a nearly shear state), and (*4*) transmission bar.

Important factors that determine the development of spatial self-organization of plastic strain localization bands are the nucleation rate and growth rate of shear bands, as well as the characteristic times of interaction between the bands [20–24]. The process of formation and development of localized shear bands was analyzed in [25, 26], which presented the experimental results on the dynamic torsion of thin-walled cylindrical specimens of structural steels on a Hopkinson–Kolsky bar. Three stages were distinguished: initial, in which plastic strain is uniform; the second stage, in which heterogeneities arise due to plastic instability; and the third stage, in which adiabatic shear bands are formed. The effects of self-organization of multiple shear bands were studied in [12, 27] for various strain rates.

The appearance of shear bands is traditionally associated with the presence of a maximum on the tensile curve. This maximum is due to the competition between stabilization due to strain hardening and destabilization due to thermal softening. There are two approaches to studying the evolution of shear bands. The first approach was developed in [21] and is based on the idea of the relationship between the diffusion of momentum and local unloading, which determines the presence of undeformable regions between the shear zones. The second approach is based on methods of perturbation theory [28].

A linear perturbation analysis was used to study the formation of localized shear bands [7]. In [20] and [9], this approach was used in the case of a one-dimensional simple shear. In [6], the model from [9] was modified to describe the strain hardening of materials. It was assumed that the wavelength corresponding to the dominant mode corresponds to the most probable minimum distance between the localized shear bands. It was concluded that the interaction between shear bands is a complex process and the distance cannot be predicted using the one-dimensional perturbation theory.

In a number of works, the evolution of the localized shear bands was represented and the distances between them was determined using the well-known phenomenological models of plasticity [29–32]: power law, Johnson–Cook model, and the MTS model.

The experimental and theoretical study whose results are presented in this article was devoted to the substantiation of the plastic strain localization mechanism established in [33, 34] under dynamic loading of materials due to the collective multiscale behavior of typical mesoscopic defects (microshears).

2. MATERIALS AND METHODS

In this work, we conducted theoretical and experimental studies of the plastic strain localization mechanisms in a nearly shear mode under dynamic loading on a split Hopkinson–Kolsky bar of specimens made of AMg6 aluminum alloy, which tends toward instability of plastic flow. For this, specimens of a special shape and equipment that provided a planar deformed state were developed and patented [35]. The temperature fields obtained on the lateral surface of the specimen allow us to judge the development of the plastic strain localization process in real time.

The thermodynamics of the deformation process, in order to identify the characteristic stages of strain localization and the development of fracture due to localized shear, was studied in situ by recording temperature fields using a CEDIP Silver 450M high-speed infrared camera, which has the following main technical characteristics: a sensitivity of at least 25 mK at 300 K, a spectral range of 3–5 μm, a maximum frame size of 320 240 pixels [36], a coordinate resolution (pixel size px) of ~0.2 mm, and a time resolution of ~0.25 ms.

It was shown in [37] that at the considered strain rates ($\sim 10^3$ s^{-1}) and higher, the characteristic times of thermal conductivity for the AMg6 alloy are significantly shorter than the characteristic times of the

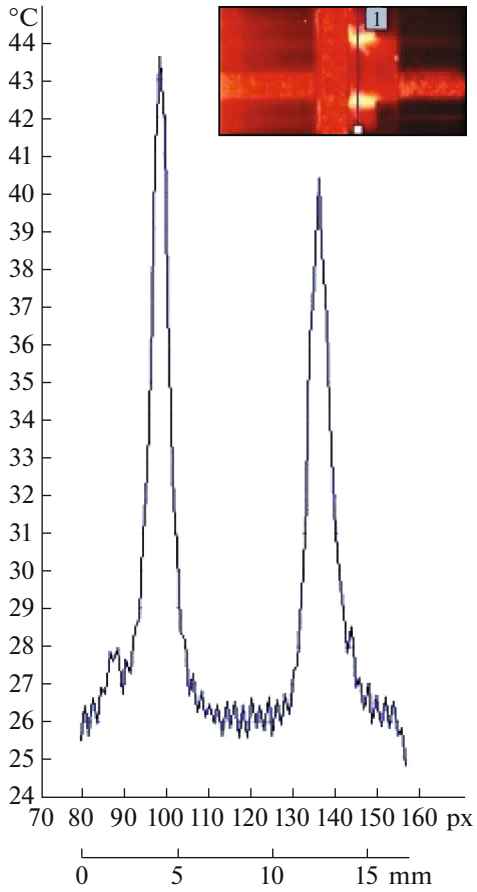

Fig. 2. An infrared image of the specimen during testing of the specimen from AMg6 alloy and temperature vs. coordinate at a selected time; the maximum temperature around the perimeter of the hole is 45°C.

deformation process. The specimen, the schematic of the experiment, and the results are presented in Figs. 1 and 2.

In situ temperature fields during deformation were obtained. Figure 2 shows an infrared image of the specimen and the dependence of temperature on the coordinate at a chosen time. The temperature field in the specimen corresponds to the moment when the temperature reaches a maximum during the test. The error of temperature measurement is ~10%. It can be seen from the figure that the temperature in the region of plastic strain localization does not exceed ~45°C. This allows us to conclude that temperature softening does not play a decisive role in the localized shear mechanism under given loading conditions.

Figure 3 shows the stress–strain diagram in the true shear stress–true shear strain coordinates, as obtained by testing on a Hopkinson–Kolsky bar for specimens of a special shape from the AMg6 alloy.

Specimens from AMg6 aluminum alloy were also tested on an original ballistic perforation device. Cylindrical projectile made of high-strength steel with a mass of 7.4 g, diameter of 5 mm, and length of 48 mm were used.

Destruction occurs upon high-speed interaction of the projectile with the target, which consists in the formation and removal of the plug. The plastic strain distribution on the rear surface of the target during fracture was studied using a CEDIP Silver 450M infrared camera. Figure 4 shows the schematics of the experiment and photographs of the perforated target from different angles, the knocked-out plug, and the projectile.

Figure 5 shows an infrared image of the hole after perforating the specimen and a graph of the temperature versus coordinate at a selected time; the projectile velocity is 417 m/s. The temperature field in the specimen is presented at the time when the temperature reaches its maximum during testing. The temperature measurement error is ~10%.

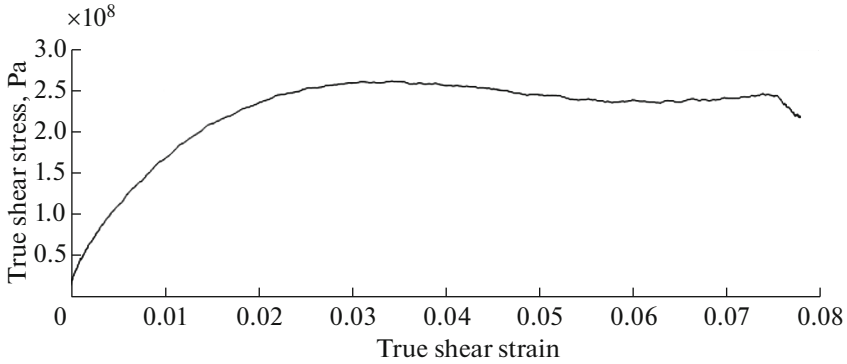

Fig. 3. True shear stress–true shear strain diagrams obtain in testing on a Hopkinson–Kola bar for specimens of a special shape from AMg6 alloy.

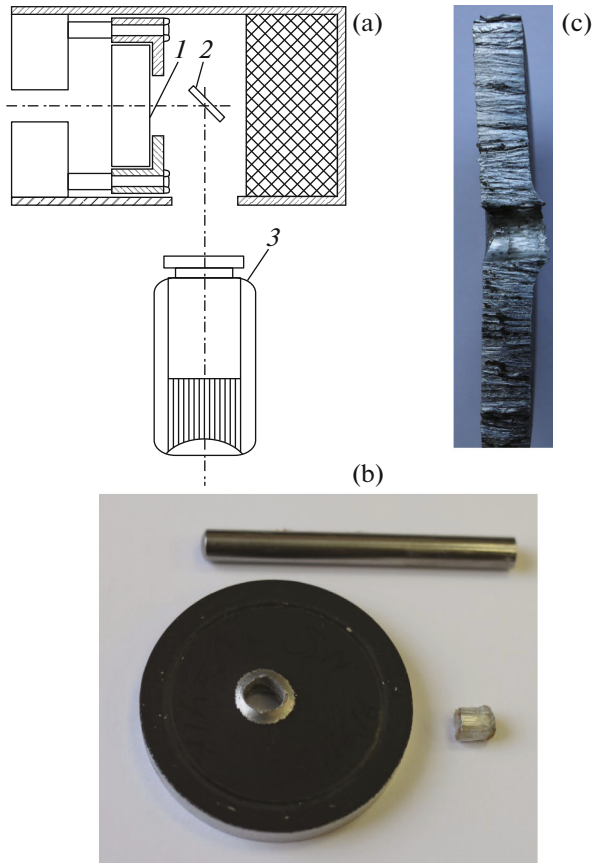

Fig. 4. (a) The schematics of the experiment: (*1*) specimen, (*2*) mirror, (*3*) infrared camera; (b) perforated target, knocked-out plug, and projectile; (c) sawed perforated target (side view).

The data obtained in the experiments with an infrared camera allow us to conclude that temperature softening did not play a decisive role in the shear localization mechanism under the given loading conditions at an average strain rate of ~5000 s^{-1}, which occurred when testing specimens of a special shape. Hereinafter, the strain rates were calculated using numerical simulation by D.A. Bilalov. The mean strain rate during target perforation was 13 900 s^{-1}. At such strain rates, along with the softening associated with the evolution of defects, temperature softening begins to have a significant effect.

The displacements and strains fields were determined experimentally during dynamic tests of specimens of special shape from the AMg6, D16, and Steel 3 alloys, developed to study the plastic strain local-

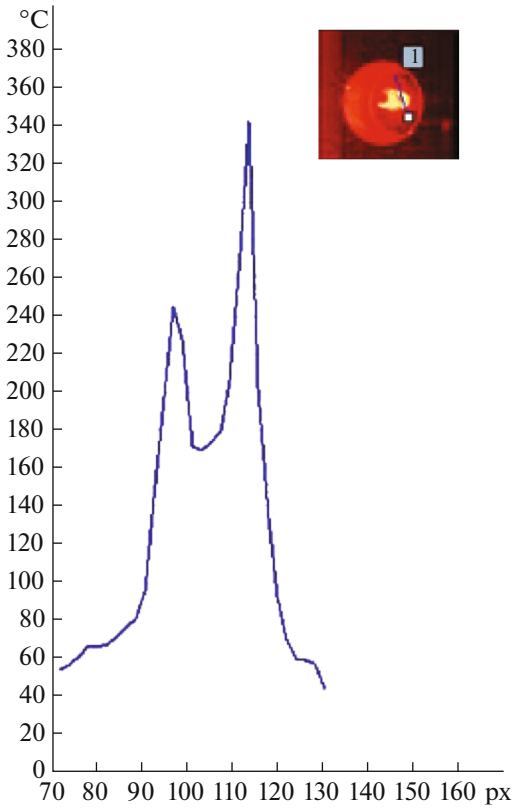

Fig. 5. An infrared image of a specimen from AMg6 alloy during testing and temperature vs. coordinate at a selected time; the maximum temperature around the perimeter of the hole is 340°C.

ization [35], on a split Hopkinson–Kolsky bar using the StrainMaster system. The displacement fields were established before and after deformation on the Hopkinson–Kolsky bar. These fields were later used to determine the deformation fields. The errors in measuring the displacement and shear strain fields were ~5%.

The results of the tests are presented in Figs. 8a 8c, and 8e.

3. NUMERICAL SIMULATION

The complete system of field equations for describing the deformation behavior of a material has the following form [36–40]:

$$\rho\dot{\mathbf{v}} = \nabla\cdot\boldsymbol{\sigma}, \tag{1}$$

$$\dot{\rho} + \rho\nabla\cdot\mathbf{v} = 0, \tag{2}$$

$$\mathbf{D} = \frac{1}{2}(\nabla\mathbf{v} + \mathbf{v}\nabla), \tag{3}$$

$$\boldsymbol{\sigma}^R = \lambda I_1(\mathbf{D}) + 2G(\mathbf{D} - \mathbf{D}^{pl} - \dot{\mathbf{p}}), \tag{4}$$

$$\mathbf{D}^{pl} = \dot{\varepsilon}_0^{n_\varepsilon}\exp\left(\frac{U(T)}{kT}\right)\left(\Gamma_\sigma\boldsymbol{\sigma} - \Gamma_{p\sigma}\frac{\partial F}{\partial\mathbf{p}}\right), \tag{5}$$

$$\dot{\mathbf{p}} = \dot{\varepsilon}_0^{n_p}\exp\left(\frac{U(T)}{kT}\right)\left(\Gamma_{p\sigma}\boldsymbol{\sigma} - \Gamma_p\frac{\partial F}{\partial\mathbf{p}}\right), \tag{6}$$

$$\frac{F}{F_m} = \frac{p^2}{2} - \frac{p^2}{2\delta} + c_1 p + c_2\ln(c_3 + c_4 p + p^2) - \frac{\boldsymbol{\sigma}:\mathbf{p}}{2G}, \tag{7}$$

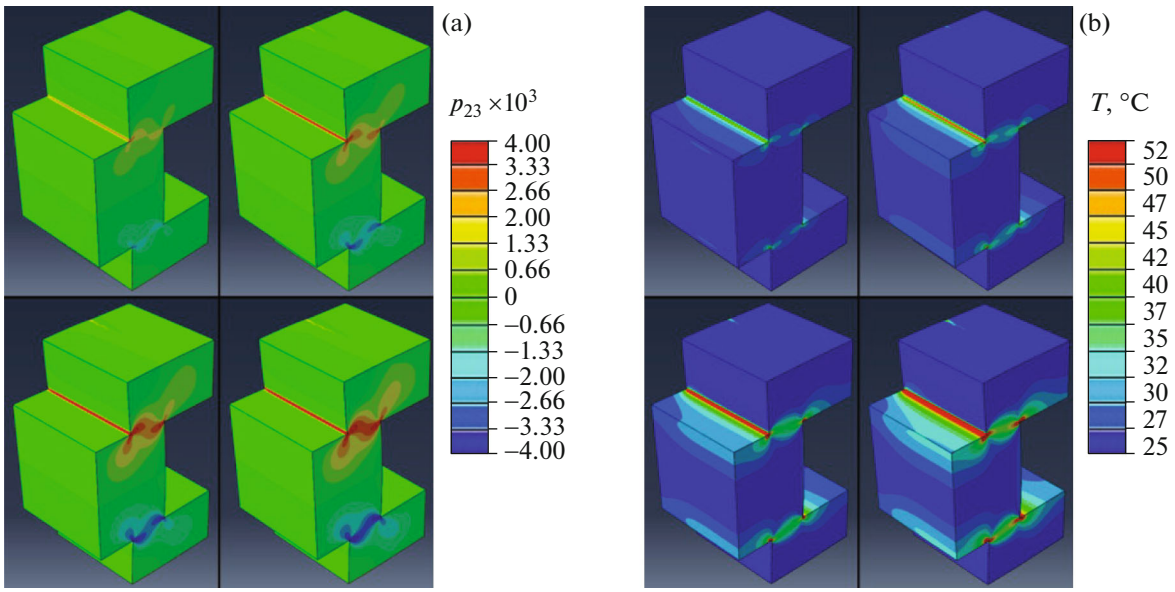

Fig. 6. The evolution of (a) the shear component of the microdefect density tensor and (b) temperature fields in the specimens whose test results are presented in Figs. 2 and 3 at different times $t \times 10^5$, s (from left to right and from top to bottom): 1.1, 2.3, 3.5, and 4.7 (3D modeling).

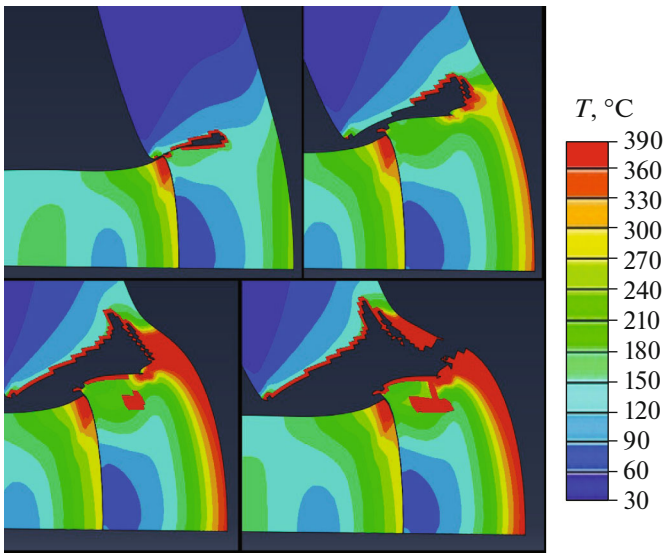

Fig. 7. The evolution of the temperature field during the removal of the plug from the specimens whose test results are presented in Figs. 4 and 5 at times $t \times 10^4$, s (from left to right and from top to bottom) 0.25, 0.5, 0.75, and 1.0 (2D modeling).

$$\rho c \dot{T} = \alpha \Delta T + \boldsymbol{\sigma} : \mathbf{D}^{pl} - \frac{\partial F}{\partial \mathbf{p}} : \dot{\mathbf{p}}, \tag{8}$$

$$\dot{\varepsilon}_0 = \frac{\sqrt{(2/3)\dot{\boldsymbol{\varepsilon}} : \dot{\boldsymbol{\varepsilon}}}}{\dot{\varepsilon}_c}, \tag{9}$$

$$p = \sqrt{\dot{\mathbf{p}} : \dot{\mathbf{p}}}, \tag{10}$$

and includes the equations of motion (1) and continuity (2), kinematic relations (3), Hooke's law in the high-speed formulation (4), kinetic equations (5) and (6), expressions for nonequilibrium free energy (7), heat equation (8), and expressions for the characteristic strain rates (9) and (10). Here, we use the

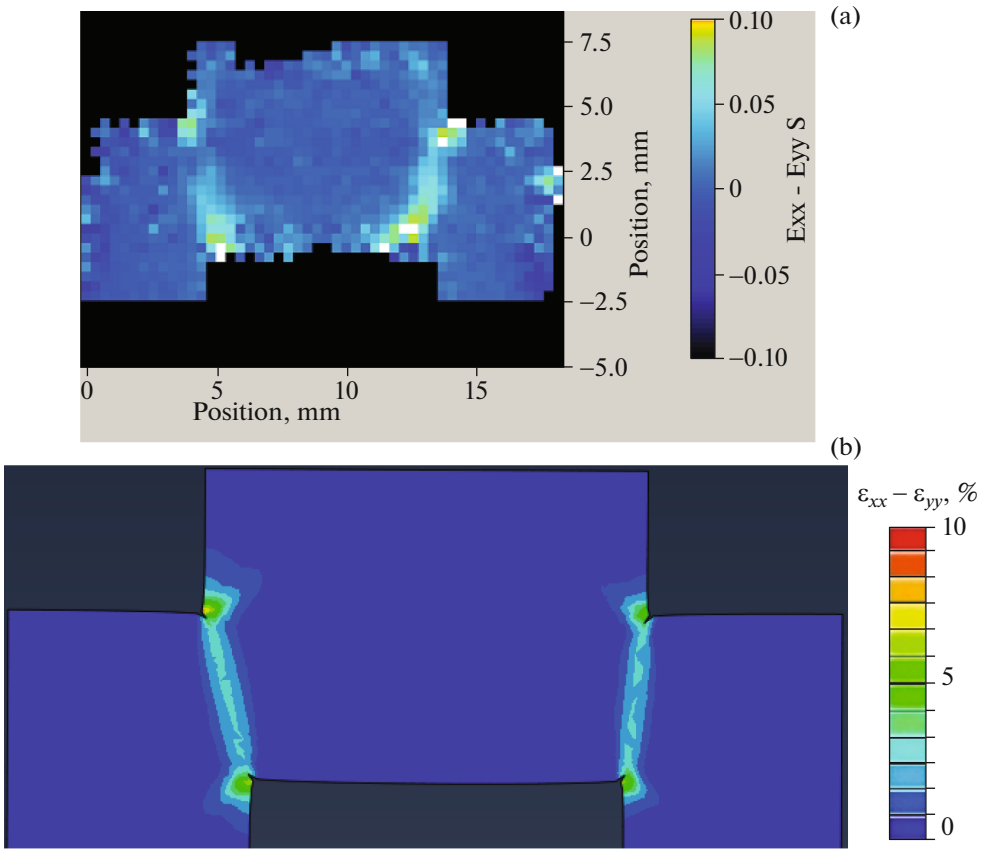

Fig. 8. The distribution of the absolute value of the strain difference $\varepsilon_{xx} - \varepsilon_{yy}$ in specimens of a special shape made of (a, b) steel St3, (c, d) AMg6 alloy, and (d, f) D16 alloy at the final time point under dynamic loading: (a) experiment and (b) numerical simulation.

following notation: ρ is the mass density; $\mathbf{v}$ is the velocity vector; $\boldsymbol{\sigma}$ is the stress tensor; $\boldsymbol{\varepsilon}$ is the strain tensor; $\mathbf{D}$ is the strain rate tensor, $\mathbf{D}^{pl}$ is its plastic component; $(\bullet)^R$ is the Green–Naghdi derivative; $I_1(\bullet)$ is the first invariant of the tensor; λ and G are the elastic characteristics of the material; $\mathbf{p}$ is the micro-shear density tensor; n_p and n_ε are constants responsible for the speed sensitivity of the material; $U(T)$ is characteristic activation energy; T is temperature; k is the Boltzmann constant; Γ_σ, $\Gamma_{p\sigma}$, and Γ_p are the kinetic coefficients; F is the nonequilibrium free energy; δ is the structural scaling parameter; F_m and c_1–c_4 are potential approximation constants; c is specific heat; α is the thermal conductivity; and $\dot{\varepsilon}_c$ is a nondimensionalization parameter equal to 1 s^{-1}. A dot over the symbols indicates a material derivative. The system of equations (1)–(10) describes the deformation behavior of plastic materials (metals and alloys) in the range of strain rates 10^{-4}–10^3 s^{-1}, taking the kinetics of defects and thermal softening into account.

The model parameters were determined by solving the problem of minimizing the discrepancy between the experimental and theoretical strain diagrams at various strain rates. The constants for the AMg6 and D16 alloys were previously determined in [38, 40], and the constants for the St3 steel were as follows: $\rho = 7840$ kg/m^3, $G = 82$ GPa, $\lambda = 104$ GPa, $\Gamma_\sigma = 496000$ (Pa s)$^{-1}$, $\Gamma_{p\sigma} = 56000$ (Pa s)$^{-1}$, $\Gamma_p = 39000$ (Pa s)$^{-1}$, $n_p = 0.94$, $n_\varepsilon = 0.94$, $U(T) \equiv 0$ (in the temperature range considered, the thermal softening of the St3 steel is negligible), $c = 450$ J/(kg K), and $\alpha = 55$ W/(m deg).

The results of numerical simulations of the experiments on loading specimens presented in Figs. 2–5 are shown in Figs. 6 and 7. The calculated temperature fields on the surface of the specimens during deformation agree with the experimental data with an accuracy of ~20%.

Specimens of the Steel 3, AMg6, and D16 alloys of special shapes were experimentally studied on a split Hopkinson–Kolsky bar using the StrainMaster non-invasive strain measurement system and numerical simulation of these experiments was carried out. The test and simulation data are presented in Fig. 8. The numerically calculated strain fields agrees with the experimental ones within 20%.

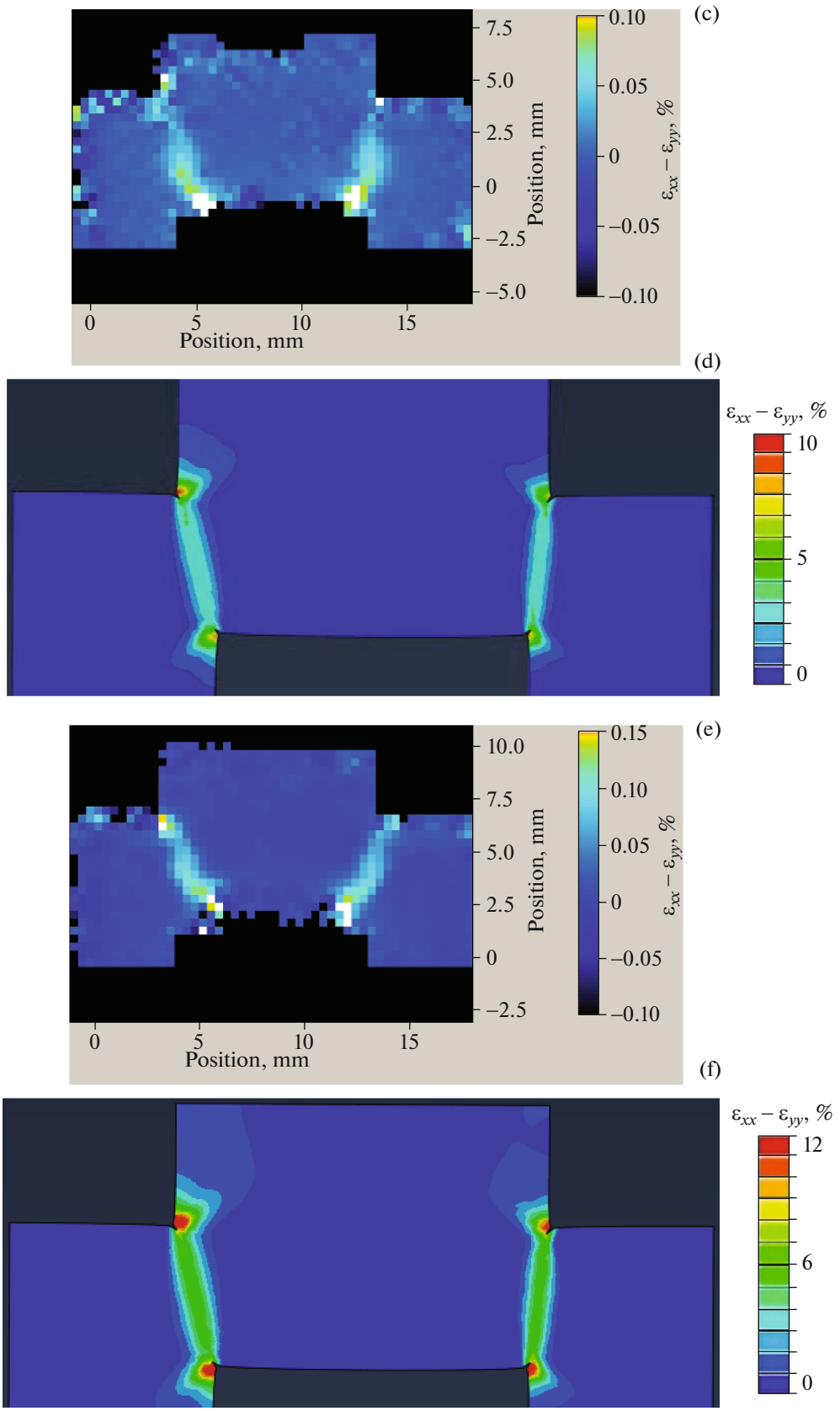
(c)
7.5
5.0
2.5
0
−2.5
−5.0
Position, mm
0
5
10
15
Position, mm
0.10
0.05
0
−0.05
−0.10
$\varepsilon_{xx} - \varepsilon_{yy}$, %
(d)
$\varepsilon_{xx} - \varepsilon_{yy}$, %
10
5
0
(e)
10.0
7.5
5.0
2.5
0
−2.5
Position, mm
0
5
10
15
Position, mm
0.15
0.10
0.05
0
−0.05
−0.10
$\varepsilon_{xx} - \varepsilon_{yy}$, %
(f)
$\varepsilon_{xx} - \varepsilon_{yy}$, %
12
6
0

Fig. 8. (Contd.)

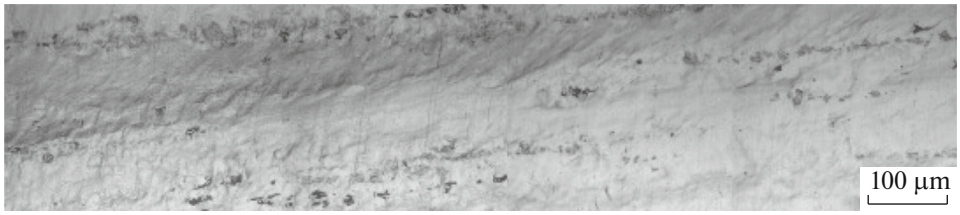

Fig. 9. An optical image of the surface of a specimen of a special shape, whose test results are presented in Figs. 2 and 3, after loading.

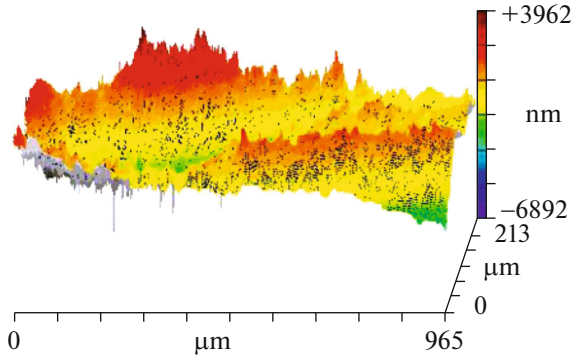

Fig. 10. The 3D image of the surface of a specimen of a special shape, whose test results of are presented in Figs. 2 and 3, after loading.

4. STUDY OF THE SURFACE RELIEF OF DEFORMED SPECIMENS

The consistency of theoretical assumptions about the leading role of multiscale mechanisms of structural relaxation due to the collective behavior of ensembles of defects in the development of plastic flow localization and fracture was studied by a structural analysis of the morphology of the surface relief. For this purpose, a NewView-5010 optical profiler was used. The data obtained with it served as a basis for calculating the scale invariant (Hurst exponent) and the spatial scale of the region in which correlated behavior of microshears is observed. Based on the value of the Hurst exponent of deformation defect structures, a physical explanation of the universality of critical phenomena can be given in relation to the fracture scenarios of various classes of materials and the influence of the state of the structure (including that formed by dynamic actions) on the threshold characteristics of the transition of a plastically deformed material to fracture.

The lateral surface of the specimen was polished before testing. The surface relief (Fig. 9) in the region of maximum shear strains (before and after loading) was registered using an interferometer-profiler (at magnification of 500×) (Fig. 10) and then analyzed by fractal analysis methods in order to determine the conditions for the correlated behavior of multiscale defect structures.

Within each 965 × 213 μm window, 10–12 profiles were studied: this number provided representativeness of the data on the relief structure induced by defects with a resolution of ~0.1 nm vertically and ~0.1 μm horizontally.

From the one-dimensional relief profiles of the fracture surface (Fig. 10), the function $K(r)$ was calculated using the formula [41]

$$K(r) = \left\langle \left(z(x+r) - z(x)\right)^2 \right\rangle_x^{1/2} \propto r^H,$$

which is the averaged difference in the heights of the surface relief $z(x+r)$ and $z(x)$ on a window of size r, where H is the Hurst exponent.

The representation of the function $K(r)$ in logarithmic coordinates (Fig. 11) allows us to estimate the structural scaling index (Hurst exponent) for a specimen of a special shape, whose test results are presented in Figs. 2 and 3, as a spatial invariant determined by a constant slope of the dependence of $\log_2 K(r)$ on $\log_2(r)$.

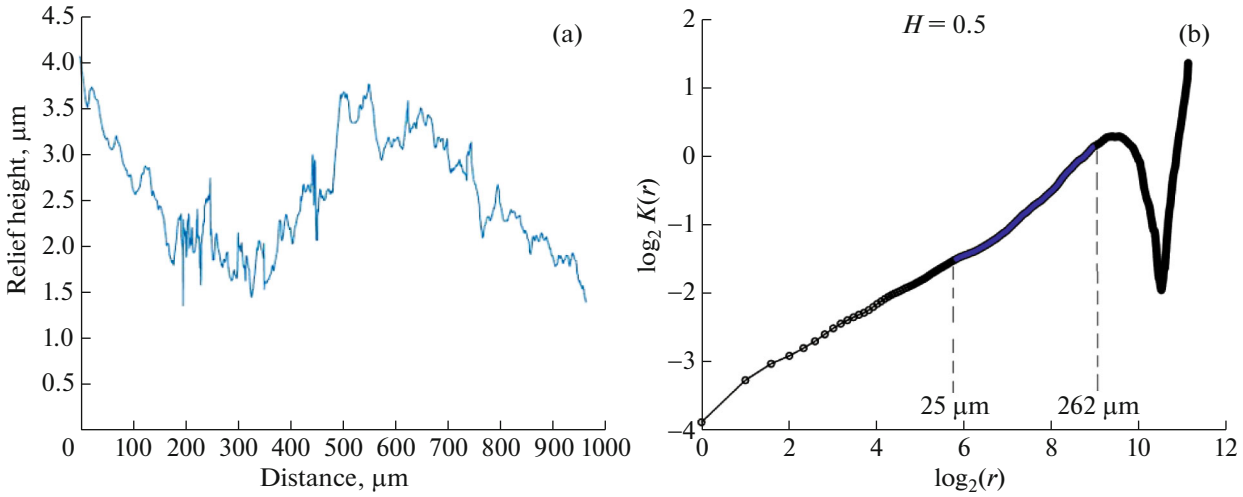

Fig. 11. (a) A typical one-dimensional profile and (b) $\log_2 K(r)$ vs. $\log_2(r)$ for the surface after deformation.

A comparative analysis of the scale-invariant characteristics of dynamically loaded specimens revealed a significant increase in the Hurst exponent (up to $H \sim 0.5$) in a wide range of spatial scales 25–262 μm, in contrast to undeformed specimens ($H \sim 0.2$) in the range of spatial scales 1–6 μm for a specimen of a special shape, whose test results are presented in Figs. 2 and 3. More substantial results can be associated with a change in both the lower and upper scales, which reflects the features of strain localization. The values of the spatial scale can be used to predict fracture kinetics under various types of loading [42].

5. CONCLUSIONS

The temperature fields established during dynamic tests of the AMg6 alloy on a Hopkinson–Kolsky bar and in target perforation using infrared thermography, the results of dynamic experiments using the StrainMaster system, the study of the structure of deformed specimens [36–40], as well as the results of numerical simulation carried out taking the mesodefect accumulation kinetics in the material into account [36–40], suggest that one of the plastic strain localization mechanisms for the considered materials under these loading conditions is not related to thermoplastic instability, but is caused by jump-wise processes in the defect structure of the material.

FUNDING

This work was supported in part by the Russian Foundation for Basic Research (projects nos. 17-08-00905_a, 17-41-590149r_a, 17-01-00867_a, 18-08-01186_a, and 19-48-590009r_a).

REFERENCES

1. Grady, D.E. and Kipp, M.E., The growth of unstable thermoplastic shear with application to steady-wave shock compression in solids, *J. Mech. Phys. Solids,* 1987, vol. 35, pp. 95–119. https://doi.org/10.1016/0022-5096(87)90030-5
2. Bai, Y.L., Thermo-plastic instability in simple shear, *J. Mech. Phys. Solids,* 1982, vol. 30, pp. 195–207. https://doi.org/10.1016/0022-5096(82)90029-1
3. Clifton, R.J., Duffy, J., Hartley, K.A., and Shawki, T.G., On critical conditions for shear band formation at high strain rates, *Scr. Metall.,* 1984, vol. 18, pp. 443-448. https://doi.org/10.1016/0036-9748(84)90418-6
4. Molinari, A., Instabilité thermoviscoplastique en cisaillement simple, *J. Mec. Theor. Appl.,* 1985, vol. 4, no. 5, pp. 659–684.
5. Molinari, A., Shear band analysis, *Solid State Phenom.,* 1988, vols. 3–4, pp. 447–467. http://www.scientific.net/SSP.3-4.447.
6. Molinari, A., Collective behavior and spacing of adiabatic shear bands, *J. Mech. Phys. Solids,* 1997, vol. 45, pp. 1551–1575. https://doi.org/10.1016/S0022-5096(97)00012-4

7. Molinari, A. and Clifton, R.J., Localisation de la déformation viscoplastique en cisaillement simple, résultats exacts en théorie non-linéaire, *C.R. Acad. Sci., Ser. II,* 1983, vol. 296, pp. 1–4.
8. Wright, T.W., Shear band susceptibility: Work hardening materials, *Int. J. Plast.,* 1992, vol. 8, pp. 583–602. https://doi.org/10.1016/0749-6419(92)90032-8
9. Wright, T.W. and Ockendon, H., A scaling law for the effect of inertia on the formation of adiabatic shear bands, *Int. J. Plast.,* 1996, vol. 12, pp. 927–934. https://doi.org/10.1016/S0749-6419(96)00034-4
10. Wright, T.W. and Walter, J.W., On stress collapse in adiabatic shear bands, *J. Mech. Phys. Solids,* 1987, vol. 35, pp. 701–720. https://doi.org/10.1016/0022-5096(87)90051-2
11. Zhou, F., Wright, T.W., and Ramesh, K.T., The formation of multiple adiabatic shear bands, *J. Mech. Phys. Solids,* 2006, vol. 54, pp. 1376–1400. https://doi.org/10.1016/j.jmps.2006.01.006
12. Yang, Y., Zeng, Y., and Gao, Z.W., Numerical and experimental studies of self-organization of shear bands in 7075 aluminium alloy, *Mater. Sci. Eng. A,* 2008, vol. 496, pp. 291–302. https://doi.org/10.1016/j.msea.2008.07.043
13. McDowell, D.L., A perspective on trends in multiscale plasticity, *Int. J. Plast.,* 2010, vol. 26, pp. 1280–1309. https://doi.org/10.1016/j.ijplas.2010.02.008
14. Austin, R.A. and McDowell, D.L., A dislocation-based constitutive model for viscoplastic deformation of FCC metals at very high strain rates, *Int. J. Plast.,* 2011, vol. 27, pp. 1–24. https://doi.org/10.1016/j.ijplas.2010.03.002
15. Bronkhorst, C.A., Cerreta, E.K., Xue, Q., Maudlin, P.J., Mason, T.A., and Gray, G.T., An experimental and numerical study of the localization behavior of tantalum and stainless steel, *Int. J. Plast.,* 2006, vol. 22, pp. 1304–1335. https://doi.org/10.1016/j.ijplas.2005.10.002
16. Cerreta, E.K., Frank, I.J., Gray, G.T., Trujillo, C.P., Korzekwa, D.A., and Dougherty, L.M., The influence of microstructure on the mechanical response of copper in shear, *Mater. Sci. Eng. A,* 2009, vol. 501, pp. 207–219. https://doi.org/10.1016/j.msea.2008.10.029
17. Rittel, D., Wang, Z.G., and Merzer, M., Adiabatic shear failure and dynamic stored energy of cold work, *Phys. Rev. Lett.,* 2006, vol. 96, p. 075502. https://doi.org/10.1103/PhysRevLett.96.075502
18. Rittel, D., A different viewpoint on adiabatic shear localization, *J. Phys. Appl. Phys.,* 2009, vol. 42, p. 214009. https://doi.org/10.1088/0022-3727/42/21/214009
19. Osovski, S., Nahmany, Y., Rittel, D., Landau, P., and Venkert, A., On the dynamic character of localized failure, *Scr. Mater.,* 2012, vol. 67, pp. 693–695. https://doi.org/10.1016/j.scriptamat.2012.07.001
20. Grady, D.E., Properties of an adiabatic shear-band process zone, *J. Mech. Phys. Solids,* 1992, vol. 40, pp. 1197–1215. https://doi.org/10.1016/0022-5096(92)90012-Q
21. Grady, D.E. and Kipp, M.E., The growth of unstable thermoplastic shear with application to steady-wave shock compression in solids, *J. Mech. Phys. Solids,* 1987, vol. 35, pp. 95–119. https://doi.org/10.1016/0022-5096(87)90030-5
22. Nesterenko, V.F., Meyers, M.A., and Wright, T.W., Self-organization in the initiation of adiabatic shear bands, *Acta Mater.,* 1998, vol. 46, pp. 327–340. https://doi.org/10.1016/S1359-6454(97)00151-1
23. Nesterenko, V.F., Xue, Q., and Meyers, M.A., Self-organization of shear bands in Ti, Ti–6%Al–4%V, and 304 stainless steel, *J. Phys. IV (France),* 2000, vol. 10, pp. Pr9-269–Pr9-274. https://doi.org/10.1051/jp4:2000945
24. Xue, Q., Meyers, M.A., and Nesterenko, V.F., Self-organization of shear bands in titanium and Ti–6Al–4V alloy, *Acta Mater.,* 2002, vol. 50, pp. 575–596. https://doi.org/10.1016/S1359-6454(01)00356-1
25. Marchand, A. and Duffy, J., An experimental study of the formation process of adiabatic shear bands in a structural steel, *J. Mech. Phys. Solids,* 1988, vol. 36, pp. 251–283. https://doi.org/10.1016/0022-5096(88)90012-9
26. Giovanola, J.H., Adiabatic shear banding under pure shear loading. Part I: Direct observation of strain localization and energy dissipation measurements, *Mech. Mater.,* 1988, vol. 7, pp. 59–71. https://doi.org/10.1016/0167-6636(88)90006-3
27. Yang, Y., Zheng, H.G., Shi, Z.J., and Zhang, Q.M., Effect of orientation on self-organization of shear bands in 7075 aluminum alloy, *Mater. Sci. Eng. A,* 2011, vol. 528, pp. 2446–2453. https://doi.org/10.1016/j.msea.2010.12.050
28. Mott, N.F. and Jones, H., *The Theory of the Properties of Metals and Alloys,* New York: Dover, 1958.

29. Batra, R.C. and Chen, L., Effect of viscoplastic relations on the instability strain, shear band initiation strain, the strain corresponding to the minimum shear band spacing, and the band width in a thermoviscoplastic material, *Int. J. Plast.,* 2001, vol. 17, pp. 1465–1489. https://doi.org/10.1016/S0749-6419%2801%2900004-3
30. Johnson, G.R. and Cook, W.H., in *Proceedings of the 7th International Symposium on Ballistics, Hague, Netherlands, April 19–21, 1983,* pp. 541–547.
31. Daridon, L., Oussouaddi, O., and Ahzi, S., Influence of the material constitutive models on the adiabatic shear band spacing: MTS, power law and Johnson-Cook models, *Int. J. Solid Struct.,* 2004, vol. 41, pp. 3109–3124. https://doi.org/10.1016/j.ijsolstr.2004.01.008
32. Follansbee, P.S. and Kocks, U.F., A constitutive description of the deformation of copper based on the use of the mechanical threshold stress as an internal state variable, *Acta Metall.,* 1988, vol. 36, pp. 81–93. https://doi.org/10.1016/0001-6160(88)90030-2
33. Naimark, O.B., Collective properties of defects ensembles and some nonlinear problems of plasticity and fracture, *Fiz. Mezomekh.,* 2003, vol. 6, no. 4, pp. 39–63.
34. Naimark, O.B., Defect-induced transitions as mechanisms of plasticity and failure in multifield continua, in *Advances in Multifield Theories of Continua with Substructure,* Capriz, G. and Mariano, P., Eds., Boston: Birkhauser, 2004, pp. 75–114. https://doi.org/10.1007/978-0-8176-8158-6_4
35. Naimark, O.B., Bayandin, Yu.V., Sokovikov, M.A., Plekhov, O.A., Uvarov, S.V., Bannikov, M.V., and Chudinov, V.V., Specimen for shear test (variants) and test method for it, RF Patent No. 2011114711/28, 2013.
36. Sokovikov, M., Bilalov, D., Oborin, V., Chudinov, V., Uvarov, S., Bayandin, Y., and Naimark, O., Structural mechanisms of formation of adiabatic shear bands, *Fratt. Integr. Strutt.,* 2016, vol. 38, pp. 296–304. https://doi.org/10.3221/IGF-ESIS.38.40
37. Bilalov, D.A., Sokovikov, M.A., Chudinov, V.V., Oborin, V.A., Bayandin, Yu.V., Terekhina, A.I., and Naimark, O.B., Numerical simulation and experimental study of plastic strain localization under the dynamic loading of specimens in conditions close to a pure shear, *J. Appl. Mech. Tech. Phys.,* 2018, vol. 59, pp. 1179–1188. https://doi.org/10.1134/S0021894418070027
38. Froustey, C., Naimark, O.B., Panteleev, I.A., Bilalov, D.A., Petrova, A.N., and Lyapunova, E.A., Multiscale structural relaxation and adiabatic shear failure mechanisms, *Fiz. Mezomekh.,* 2017, vol. 20, pp. 31–42. https://doi.org/10.1134/S1029959917010039
39. Bilalov, D.A., Bayandin, Yu.V., and Naimark, O.B., Mathematical modeling of failure process of AlMg2.5 alloy during high- and very high cycle fatigue, *Vychisl. Mekh. Splosh. Sred,* 2018, vol. 11, no. 3, pp. 323–334. https://doi.org/10.7242/1999-6691/2018.11.3.24
40. Bilalov, D.A., Sokovikov, M.A., and Chudinov, V.V., Multiscale mechanisms of plastic strain localization in the process of target perforation, *Deform. Razrush. Mater.,* 2017, no. 5, pp. 43–47.
41. Bouchaud, E., Scaling properties of cracks, *J. Phys.: Condens. Matter,* 1997, vol. 9, pp. 4319–4344. https://doi.org/10.1088/0953-8984/9/21/002
42. Oborin, V.A., Bannikov, M.A., Naimark, O.B., Sokovikov, M.A., and Bilalov, D.A., Multiscale study of fracture in aluminum–magnesium alloy under fatigue and dynamic loading, *Fratt. Integr. Strutt.,* 2015, vol. 34, pp. 479–483. https://doi.org/10.3221/IGF-ESIS.34.47

Translated by E. Chernokozhin